JGR Space Physics

RESEARCH ARTICLE
10.1029/2021JA029300

Key Points:

- Doppler flash is predominantly driven by changes in ionospheric refractive index
- The F-region ionosphere contributes significantly to the Doppler flash
- Lowering of the F-region reflection height is due to the flare-driven weakening of upward ion-drift

Correspondence to:
S. Chakraborty,
shibaji7@vt.edu

Citation:
Chakraborty, S., Qian, L., Ruohoniemi, J. M., Baker, J. B. H., Mclnerney, J. M., & Nishitani, N. (2021). The role of flare-driven ionospheric electron density changes on the Doppler flash observed by SuperDARN HF radars. *Journal of Geophysical Research: Space Physics*, *126*, e2021JA029300. https://doi.org/10.1029/2021JA029300

Received 3 MAR 2021
Accepted 30 JUL 2021

The Role of Flare-Driven Ionospheric Electron Density Changes on the Doppler Flash Observed by SuperDARN HF Radars

S. Chakraborty[1], L. Qian[2], J. M. Ruohoniemi[1], J. B. H. Baker[1], J. M. Mclnerney[2], and N. Nishitani[3]

[1]Bradley Department of Electrical and Computer Engineering, Virginia Tech, Blacksburg, VA, USA, [2]National Center for Atmospheric Research, Boulder, CO, USA, [3]Institute for Space-Earth Environmental Research, Nagoya University, Nagoya, Japan

Abstract Trans-ionospheric high frequency (HF: 3–30 MHz) signals experience strong attenuation following a solar flare-driven sudden ionospheric disturbance (SID). Solar flare-driven HF absorption, referred to as short-wave fadeout, is a well-known impact of SIDs, but the initial Doppler frequency shift phenomena, also known as "Doppler flash" in the traveling radio wave is not well understood. This study seeks to advance our understanding of the initial impacts of solar flare-driven SID using a physics-based whole atmosphere model for a specific solar flare event. First, we demonstrate that the Doppler flash phenomenon observed by Super Dual Auroral Radar Network (SuperDARN) radars can be successfully reproduced using first-principles based modeling. The output from the simulation is validated against SuperDARN line-of-sight Doppler velocity measurements. We then examine which region of the ionosphere, D, E, or F, makes the largest contribution to the Doppler flash. We also consider the relative contribution of change in refractive index through the ionospheric layers versus lowered reflection height. We find: (a) the model is able to reproduce radar observations with an root-median-squared-error and a mean percentage error (δ) of 3.72 m/s and 0.67%, respectively; (b) the F-region is the most significant contributor to the total Doppler flash (~48%), 30% of which is contributed by the change in F-region's refractive index, while the other ~18% is due to change in ray reflection height. Our analysis shows lowering of the F-region's ray reflection point is a secondary driver compared to the change in refractive index.

Plain Language Summary Sudden eruption of electromagnetic radiation from the Sun, also known as a solar flares, alters the physical properties of the ionosphere, creating ionospheric perturbations, commonly referred to as a sudden ionospheric disturbance (SID). The ionosphere perturbation following a solar flare disrupts the over the horizon radio communication channels on the dayside of the Earth, also known as shortwave fadeout. The ionospheric radio wave absorption effect during a solar flare-driven SID is a well known and understood phenomena. However, the initial Doppler frequency shift, also known as "Doppler flash," in the traveling radio wave is a newly discovered phenomena and not yet fully understood. This paper seeks to advance our understanding of the initial impacts of solar flares on the ionospheric properties.

1. Introduction

A solar flare is a sudden intensification of the Sun's electromagnetic radiation, specifically in the EUV and X-ray wavebands of the solar spectrum, that lasts for a few tens of minutes to several hours (e.g., Hansen & Kleczek, 1962; Rastogi et al., 1999; Siskind et al., 2017). The intensification of solar electromagnetic radiation during a solar flare enhances the plasma density via photoionization in the dayside of the Earth's ionosphere that leads to sudden ionospheric disturbances (SIDs) (e.g., Davies, 1990; Dellinger, 1937). SID affects trans-ionospheric high frequency (HF: 3–30 MHz) communication by disrupting the signal properties, namely, signal amplitude (e.g., Chakraborty et al., 2018; Davies, 1990), frequency (Kikuchi et al., 1986; Watanabe & Nishitani, 2013), and phase (e.g., Khan et al., 2005). Disruption of HF signal amplitude following SIDs, is commonly referred to as shortwave fadeout (SWF) (e.g., Chakraborty et al., 2019; Fiori et al., 2018), while disruptions of signal frequency and phase are known as sudden frequency deviation

(SFD) (e.g., Liu et al., 1996) and sudden phase anomaly (e.g., Khan et al., 2005), respectively. Disruption of signal amplitude or SWF has been a topic of research for almost a century and has produced hundreds of publications. In contrast, the relatively newly discovered phenomenon of SFD that occurs during the initial phase of SID is not well understood. The manifestation of SFD signature in HF radar observations is a sudden rise in the apparent Doppler velocity of the backscatter signal, commonly referred to as the "Doppler flash." Chakraborty et al. (2018) showed that the Doppler flash is the earliest signature recorded by HF radar during a flare-driven SID event. A detailed study of Doppler flash can enable us to gain insight about the spatiotemporal evolution of flare-driven HF absorption and unveil knowledge into ionospheric electrodynamics including ionospheric conductivity, the equatorial fountain effect, the equatorial electrojet (e.g., Sumod & Pant, 2019), and the S_q current systems (e.g., Curto et al., 2018).

Historically, VLF receivers (e.g., Khan et al., 2005), and ionosondes (e.g., Ellison, 1953) have been the primary instruments used to study SFDs. Incoherent scatter radar (ISR) (e.g., Mendillo & Evans, 1974; Pedatella et al., 2019), and Super Dual Auroral Radar Network (SuperDARN HF radars) (e.g., Fiori et al., 2018; Watanabe & Nishitani, 2013) have been used to study solar flare-driven Doppler anomalies in the ionosphere. While ionosondes and VLF receivers provide information about ionospheric plasma density enhancement, the ISRs observe changes in a more complete set of ionospheric properties, namely, ionospheric temperature, plasma density, and ion-drift parameters. Some studies exploit data from ISRs and magnetometers to study changes in the ionospheric S_q current system (e.g., Alken & Maus, 2010). In comparison, SuperDARN radars observe a sudden rise in Doppler velocity in the backscatter signal, which can provide insights into propagation conditions in the ionosphere. Although SuperDARN HF radars are affected severely by radio-blackout during the peak of HF absorption (e.g., Chakraborty et al., 2018), they can be used to study the spatiotemporal evolution of the initial and recovery phases of SIDs.

Prior studies have suggested that the Doppler flash is caused by a sudden change in the phase path length of the traveling radio waves (e.g., Kikuchi et al., 1986; Watanabe & Nishitani, 2013). Kikuchi et al. (1986) suggested two possible sources that might contribute to the change in phase path length: first, change in refractive index due to the enhancement of plasma density in the non-deviative part of the ionosphere, that is, D and lower E-regions; and second, change in the F-region ray reflection height. They postulated that change in the F-region ray reflection height is associated more with geomagnetic storms and traveling ionospheric disturbances while the change in refractive index of the non-deviative slab of the ionosphere is predominantly due to enhanced photoionization following a solar flare. In a statistical study, Watanabe and Nishitani (2013) showed that the Doppler flash originating from a solar flare is predominately driven by changes in the ionospheric refractive index. However, that study did not discuss which region of the ionosphere is primarily responsible for the Doppler flash phenomenon.

Clearly, we do not have a robust understanding of the sources and driving mechanisms of the flare-driven Doppler flash phenomenon. Observations and modeling efforts regarding the manifestation and evolution of the Doppler flash are very limited. Our primary objective in this study is to demonstrate that first-principles based modeling of HF signal propagation through the flare-modified ionosphere can reproduce radar observations. Next we applied the results to answer the following questions: (a) Is the Doppler Flash primarily a D and lower E-region phenomenon? (b) Does a solar flare impact the HF signal through the height change of the F-region? and (c) What drives the change in F-region ray reflection height? We present a comprehensive data-model analysis of the Doppler flash that follows an X-class solar flare. Specifically, we used the Flare Irradiance Spectrum Model (FISM) to capture flare-time changes in the solar spectrum and the Whole Atmosphere Community Climate Model with thermosphere and ionosphere extension (WACCM-X) to simulate the flare-enhanced electron density. We then used a ray-tracing model, Provision of High-Frequency Ray-tracing Laboratory for Propagation Studies (PHaRLAP), to geolocate HF rays. Finally, we used the Doppler model described by Kikuchi et al. (1986) to calculate the Doppler flash and compare it with the SuperDARN radar observations. This paper is organized as follows: Section 2 provides a brief introduction to the instruments and datasets used in the study; Section 3 describes different models used in this study; Section 4 presents model results, comparison of the model results with observations, and a statistical study examining sources of the Doppler flash; Section 5 provides discussion of the results in the context of similar work.

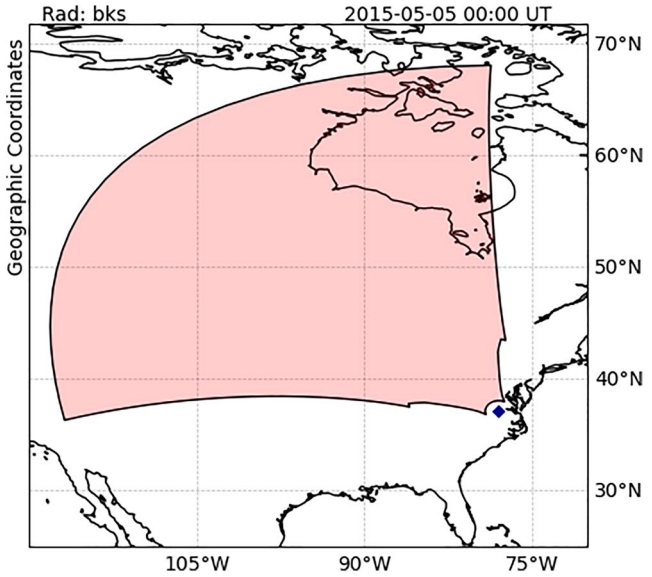

Figure 1. Field-of-view of the SuperDARN Blackstone radar located at middle latitude used in this study.

2. Instrumentation and Datasets

SuperDARN is a network of HF radars, operating between 8 and 18 MHz, distributed across the middle, high, and polar latitudes of both hemispheres. Each radar measures the line-of-sight (LoS) component of the $\vec{E} \times \vec{B}$ drift velocity of decameter-scale ionospheric plasma irregularities (e.g., Chisham et al., 2007; Greenwald et al., 1985; Nishitani et al., 2019). The field-of-view (FoV) typically comprises 16–20 azimuth beams and in 75–110 range gates spaced 45 km apart beginning in the 180 km range. Typical integration time of each beam sounding is 3-s or 6-s, which results in a full radar sweep through all beams in 1 or 2 min. Figure 1 shows the location of the SuperDARN Blackstone radar and its FoV.

SuperDARN observations primarily consist of two types of backscatter, namely, ionospheric scatter and ground scatter. Figure 2 presents an illustration of the generating mechanisms and an example of a Doppler velocity FoV plot of ground and ionospheric scatter data. In the case of ground scatter (corresponds to Ray (1) in Figure 2a), due to the high daytime vertical gradient in the refractive index, the rays bend toward the ground and are reflected from surface roughness and return to the radar following the same paths. This simulates a one-hop ground-to-ground communication link that passes through the D-region 4 times. Ionospheric scatter (corresponds to Ray (2) of Figure 2a) is due to the reflection of the transmitted signal from ionospheric plasma irregularities. Typically, ground and ionospheric scatters are associated with relatively lower & higher Doppler velocities and narrower & wider spectral widths, respectively. Figure 2b presents a SuperDARN FoV Doppler velocity scan plot from the Blackstone radar showing ground scatter (in gray) and ionospheric scatter (color coded by Doppler velocity). Daytime SuperDARN observations typically consist of a band of ground scatter that extends over several hundred kilometers in range. The effects of solar flares can be easily identified as a sudden bite-out in the daytime ground scatter band and so we will only use the ground scatter observations in this study. Doppler LoS velocity of the backscatter signal is one of the primary data products of SuperDARN radars. The Doppler velocity is obtained from the Doppler shift in the backscattered signal frequency. Increased backscattered signal frequency or blueshift signifies apparent movement towards the radar and is identified as a positive Doppler velocity. Decreased backscattered signal frequency or redshift signifies apparent movement away from the radar and is identified as a negative Doppler velocity.

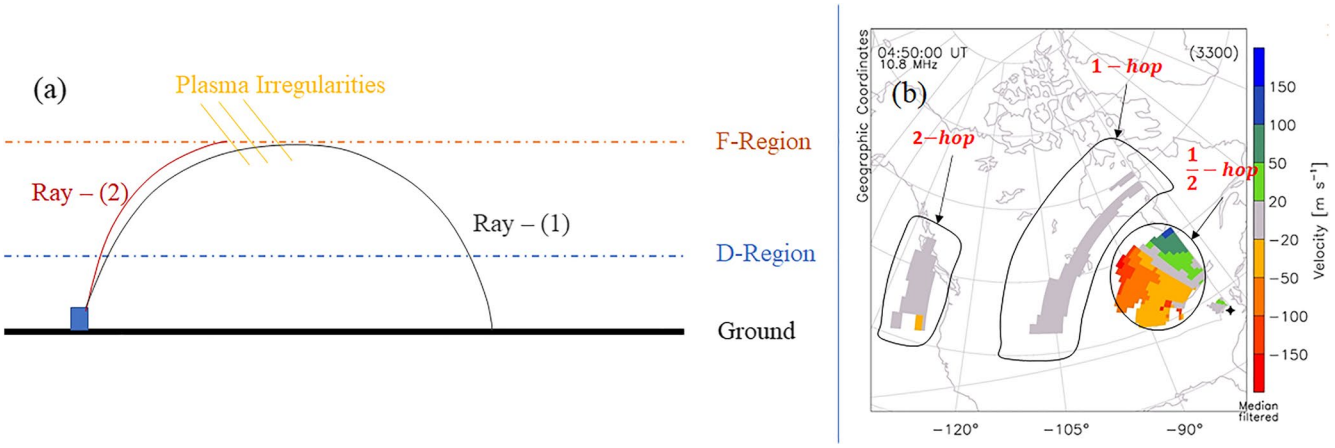

Figure 2. (a) Schematic plot of SuperDARN radar ray paths of ground scatter and ionospheric scatter, (b) SuperDARN field-of-view scan plot, showing line-of-sight Doppler velocity measured by the Blackstone radar on March 17, 2015 at 4:50 UT. Velocity is color coded according to the scale on the right and ground scatter is marked gray. Different hops of scatter are identified and tagged by the enclosed regions and texts in red.

3. Models

In this section we describe the combinations of models used to numerically estimate the Doppler flash. We used a combination of four models, namely FISM, WACCM-X, PHaRLAP ray-tracing, and Kikuchi's Doppler model. The FISM and WACCM-X models provide estimates of enhanced solar irradiance and ionospheric electron density following a solar flare. The PHaRLAP ray-tracing model is used to geo-locate trans-ionospheric HF waves. Finally, we apply the Doppler theory described by Kikuchi et al. (1986) to estimate Doppler frequency shifts experienced by the traveling HF radio waves and the associated velocities measured by SuperDARN radars.

3.1. Flare Irradiance Spectral Model: FISM

The FISM is an empirical model that estimates the solar irradiance at wavelengths from 0.1 to 190 nm at 1 nm resolution with a time cadence of one day (Chamberlin et al., 2008) and 60s (Chamberlin et al., 2007). FISM with time resolutions of one day and 60 s are referred to as the daily and flare component, respectively. The FISM flare component algorithm is parameterized by F10.7 and outputs 1-min high resolution solar irradiance data. This high resolution data are used by ionospheric general circulation models to reproduce the flare time dynamics. FISM is built on Solar EUV Experiment (SEE) data, modified by the GOES 3-s data as a solar flare proxy. The FISM flare component predicts the solar irradiance variations from both the impulsive and gradual phases of solar flares. FISM outputs quantify the changes in solar irradiance that directly affect satellite drag and radio communications, as well as the accuracy in the Global Positioning System (GPS).

3.2. WACCM-X Model

Whole Atmosphere Community Climate Model with thermosphere and ionosphere extension or WACCM-X is WACCM with an extension into the thermosphere/ionosphere. WACCM is a whole atmosphere climate-chemistry general circulation model, with an upper boundary at ∼140 km (Garcia et al., 2007; Marsh et al., 2013; Neale et al., 2013). It is a configuration of the NCAR Community Earth System Model (Hurrell et al., 2013). WACCM chemistry is based on the MOZART Model (Kinnison et al., 2007) (The Model for Ozone and Related Chemical Tracers), which includes all of the reactions that are known to be important for the middle and upper atmosphere. In the mesosphere and lower thermosphere region, a radiative transfer algorithm for CO_2 is employed (Fomichev et al., 1993). Detailed discussion of chemistry, radiative transfer, and other forcings such as volcanic aerosols are described in Marsh et al. (2013).

WACCM-X has a 1.9° × 2.5° horizontal resolution and a 0.25 scale height vertical resolution above 1 hPa (∼50 km), with an upper boundary at ∼600 km, depending on solar activity (Liu, Bardeen, et al., 2018; Liu et al., 2010). The thermosphere/ionosphere extension adds a self-consistent ionosphere module that includes computation of electron and ion temperatures, self-consistent solution of global electrodynamics including an interactive electric wind dynamo at mid- and low-latitudes, and O^+ transport in the ionospheric F-region. At high latitudes, the electric field of magnetospheric origin is parameterized according to Heelis et al. (1982) or Weimer (2005), or provided by the Assimilative Mapping Ionospheric Electrodynamics procedure (Lu & Richmond, 1996; Richmond, 1992). Default solar ultraviolet irradiance is parameterized by F10.7 index, or supplied by measurements (Solomon & Qian, 2005). To capture flare time solar irradiance variations, WACCM-X uses solar irradiance information from the FISM. Details of the model are described in Liu, Bardeen, et al. (2018) and Liu, Liu, et al. (2018). Additional validation and recent studies using this model can be found in Liu, Liu, et al. (2018), Pedatella et al. (2018), Qian et al. (2018), and Solomon et al. (2018, 2019).

3.3. PHaRLAP: HF Ray-Tracing Model

To geolocate the HF rays in the ionosphere we have used the PHaRLAP ray tracing model (Cervera & Harris, 2014). PHaRLAP implements a variety of ray tracing engines of varying sophistication from 2D ray tracing to full 3D magnetoionic ray tracing. The 2D and 3D ray tracing modules are the implementations of the 2D equations developed by Coleman (1997, 1998) and Haselgrove (1963) equations. In the case of 2D ray tracing the model takes ionospheric parameters, HF ray properties, elevation and bearing angle of

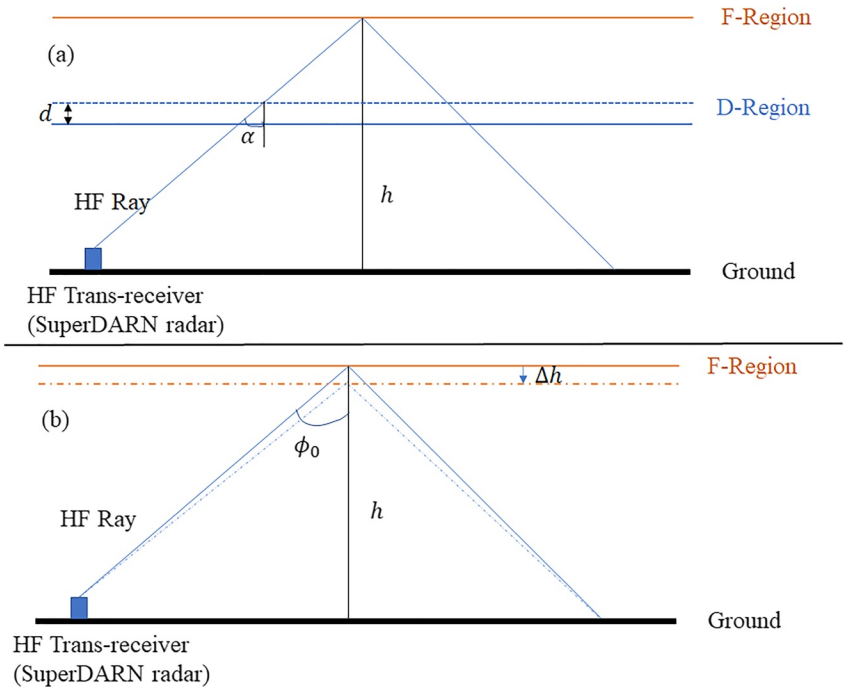

Figure 3. Illustration of two sources of Doppler shifts in the high frequency signal (Adopted from Kikuchi et al., 1986). Change in phase path length due to: (a) the change in refractive index (due to the enhanced electron density) in the non-deviative part of the ionosphere below the reflecting F-region and (b) the lowering of the F-region ray reflection height.

the ray as inputs and produces height and ground-range of the traveling HF ray in km as output. The 3D ray tracing module produces height, latitude, and longitude of the traveling HF ray as output. We used the 2D ray tracing module to geolocate rays along each individual beam of the SuperDARN Blackstone radar.

3.4. Kikuchi's Doppler Flash Model

Kikuchi et al. (1986) suggests that the following drivers are the main sources of the change in phase path length that are associated with the Doppler flash: (a) change in refractive index of the non-deviative slab of the ionosphere following a solar flare, and (or) (b) change in ray reflection height following a geomagnetic storm. Figure 3 presents an illustration of how these two drivers reduce the phase path length of the traveling radio wave. In case (a) shown in Figure 3a, Kikuchi's model assumes that the change in refractive index (η) is caused by increased ionization in the non-deviative slab with a thickness of d (D and lower E-region), electron density n_e, and ray incident angle α. The Doppler frequency shift due to the change in refractive index is mathematically described by Equation 1. We have the numerical capability to estimate the change in refractive index (η) along the raypath. Figure 3b presents case (b) of Kikuchi's Doppler model, where ϕ_0 is the angle of the incident ray and Δh is the change in reflection height. Equation 2 provides the amount of Doppler frequency shift due to the change in ray reflection height.

$$\Delta f_{d\eta} = \frac{k}{cf}\frac{dn_e}{dt}\frac{d}{\cos\alpha} \tag{1}$$

$$\Delta f_{dh} = -\frac{2f}{c}\frac{dh}{dt}\cos\phi_0 \tag{2}$$

$$\Delta v = 2c \times \frac{\sum \Delta f_*}{f} \quad (3)$$

where: c, h, ϕ_0, η, n_e, k, α, and f are the speed of light, height of the reflecting layer, incident angle at the reflecting layer, refractive index, electron density, wavenumber, incident angle at each height interval, and signal frequency, respectively. The Δf_* and Δv in Equation 3 are the change in signal frequency resulting from change in ionospheric refractive index or from change in the F-region ray reflection height and total Doppler velocity observed by the radar, respectively.

4. Results

In this section, we present a classic example of a Doppler flash event observed by the Blackstone radar in response to an X class solar flare (X2.7) on May 5, 2015 at 22:11 UT. Then, we provide simulated Doppler flash output from the model and compare it with radar observations. Finally, we present a statistical study of Doppler flash signatures observed by the Blackstone radar based on the model simulation. We will examine the relative contributions by the three ionospheric regions, D, E, and F, to the total Doppler flash. In addition, we analyze the influence of refractive index versus lowering of the reflection height on the Doppler flash.

4.1. Event Study: The Doppler Flash on May 5, 2015

On May 5, 2015 an X2.7 class solar flare erupted from the solar active region 2339. The flare started, reached its peak, and ended at 22:05 UT, 22:11 UT, and ~22:25 UT, respectively. The maximum K_p value on this UT day was 2^+, thus we conclude the background geomagnetic conditions during this flare were mild and thus suitable to study the solar flare effects on the ionosphere (Chakraborty et al., 2018). We have selected this event as an exemplar to showcase the X-class flare-driven Doppler flash phenomenon.

Figure 4 presents images of the SWF event seen by the SuperDARN Blackstone radar. The upper nine panels (Figures 4a) present a series of FoV scan plots of LoS Doppler velocity at 4-min cadence, while the bottom panel (Figure 4b) shows a range-time plot of LoS Doppler velocity for all beams. Panel 4(a)[iv] shows a complete wipeout of backscatter signal at 22:12 UT, consistent with the HF absorption phase of SWF, while Figure 4b shows that the SWF phenomenon lasted on the order of tens of minutes. The radio blackout event was preceded by a sudden enhancement of apparent backscatter Doppler velocity or a blue shift at 22:08 UT (panel 4(a)[iii]), which is also evident in Figure 4b. This feature is referred to as the Doppler flash. The observations indicate a slight negative Doppler velocity or a redshift during the recovery phase of the event. The rising phase of the solar flare Doppler flash phenomenon starts with a large frequency blue shift and is followed by a smaller but prolonged frequency redshift in the recovery phase. The location of the ground scatter band is not significantly perturbed during the Doppler flash so we can conclude that the geometry of the raypath is not greatly affected by the solar flare-driven SID.

4.2. Data-Model Comparison

This subsection describes the model outputs and compares them with the SuperDARN Blackstone radar observations. Figure 5 presents a data-model comparison for the SuperDARN Blackstone radar at the peak of the Doppler flash (May 5, 2015, 22:08 UT). The left and right panels show Doppler velocity estimated using the model and observations from the Blackstone radar, respectively. Velocity is color-coded by the color-bar on the right. To compare the modeled output against the observations we have used two difference metrics, root-median-squared-error (RMdSE) and mean percentage error (MPE, δ). The RMdSE represents the square root of medianed squared differences between predicted and observed values. The MPE represents the mean of the ratio taken between the difference in observation and modeled values and the observation. The RMdSE and MPE for this case are provided in the right panel of the figure. Note that as radar observations are affected by the initial phase of the SWF, the radar did not receive backscattered echoes for all the range-cells uniformly. Hence, to estimate RMdSE and MPE we only consider range-cells with valid observations. The region enclosed by the red dashed lines represents beam 7 of the radar. The model is able

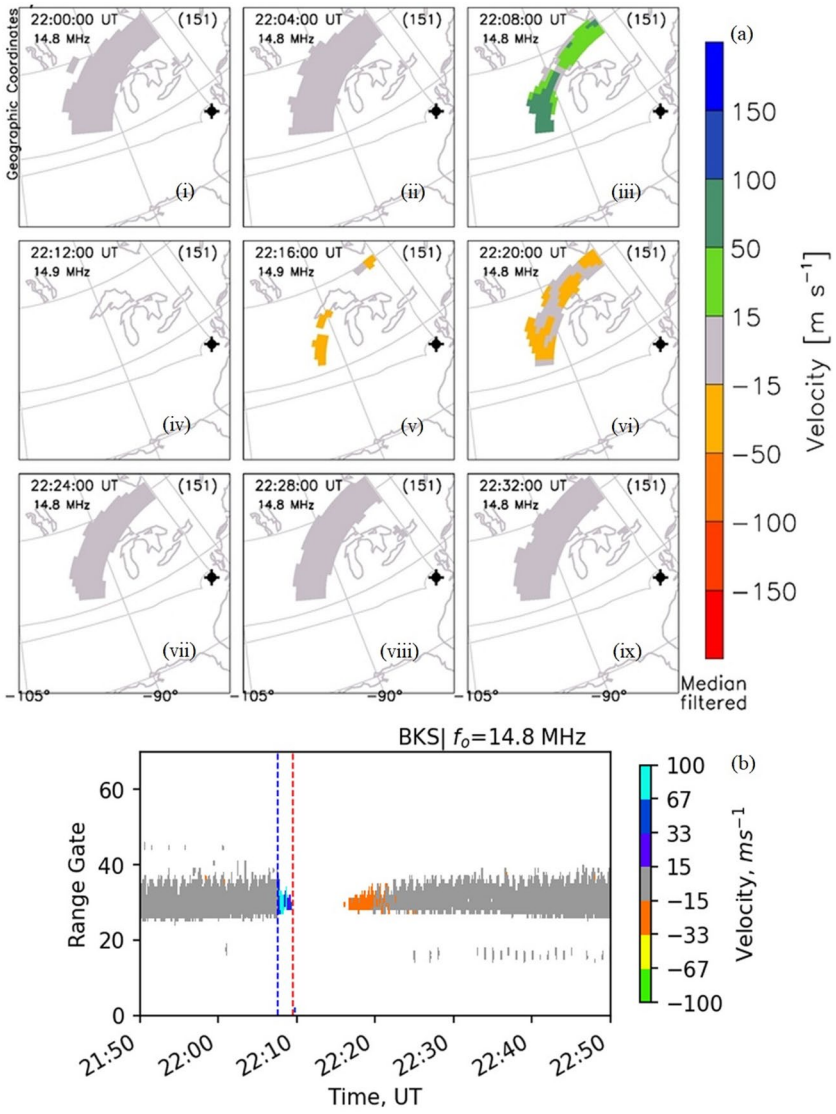

Figure 4. Response of the SuperDARN Blackstone radar to a solar flare on May 5, 2015: (a)[i-ix] Series of field-of-view scan plots showing line-of-sight Doppler velocity color coded according to the scale on the right and (b) Range-Time-Interval plot showing backscattered Doppler velocity from all beams, color coded according to the scale on the right. Blue and red vertical lines represent the start of the Doppler flash and start of the radio blackout, respectively.

to replicate the radar observations during the peak of the Doppler flash with an RMdSE of 4.51 m/s and a MPE (δ) of 1.43%. Next we will use one beam (beam 7 indicated by the red dashed line in Figure 5) to do a comprehensive data-model comparison.

Figure 6 presents the data-model comparison from beam 7 of the SuperDARN Blackstone radar observations for the 1-h time interval 21:51–22:52 UT. Panels (a) and (b) present modeled Doppler velocity contributed by the change in refractive index and change in the ray reflection height, respectively. The bottom panel (c) presents total Doppler velocity estimated using the model. The red dots in panel (c) are observations from beam 7 of the SuperDARN Blackstone radar. Error bars in all panels represent variations of Doppler velocity along beam 7. Similar to the previous comparison, we used RMdSE and MPE to validate our model predictions against the radar observations along beam 7. The radar observations are severely affected by the blackout (peak of HF absorption (Chakraborty et al., 2018)) during 22:10–22:17 UT, and thus the observations suffer from the bite-out effects of the SWF. The comparison metrics are estimated based on the available data points. The analysis indicates that the model is able to replicate velocity observations during

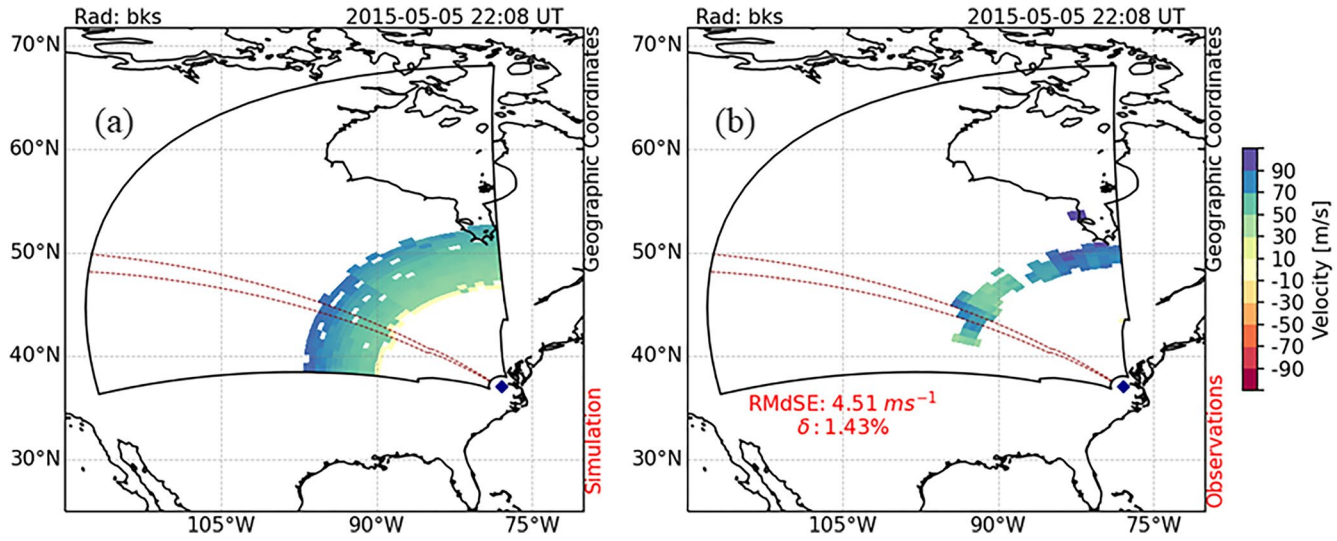

Figure 5. Data-model comparison for SuperDARN Blackstone radar measurements at the peak of the Doppler flash (22:08 UT). Field-of-view scan plots showing: (a) Doppler velocity simulated using the model and (b) observations from the Blackstone radar. Doppler velocity is color coded according to the scale on the right. Root-median-squared-error and mean percentage error δ) between modeled and observed Doppler velocity is provided in panel (b). The region enclosed by the red dashed lines represents beam 7 of the radar.

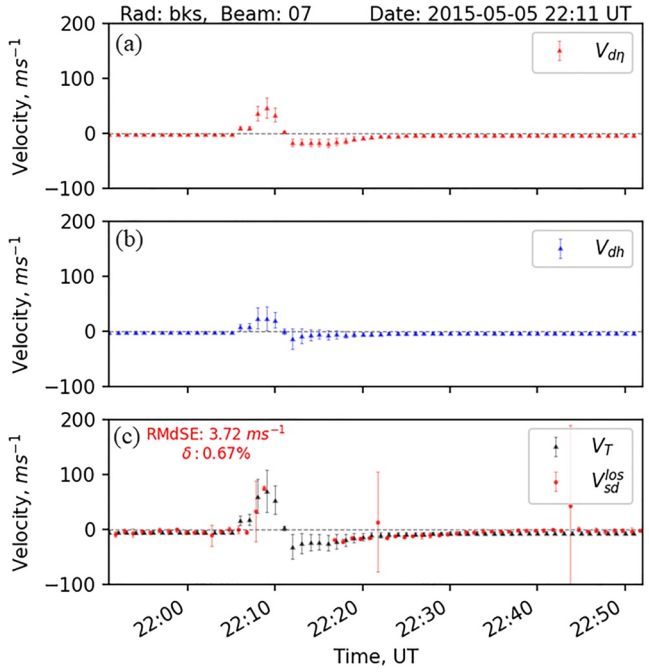

Figure 6. Time series plot of data-model comparison along beam 7 (region enclosed by the red dashed lines in Figure 5) of the SuperDARN Blackstone radar: (a) modeled Doppler velocity due to the change in refractive index, (b) modeled Doppler velocity due to the change in ray reflection height, and (c) total Doppler velocity. The red dots in panel (c) are observations from the SuperDARN Blackstone radar along beam 7. Error bars in all panels present the variation of Doppler velocity along beam 7. Root-median-squared-error (RMdSE) and mean percentage error between modeled and observed Doppler velocity are provided in panel (c). Outliers are characterized by the large uncertainty values indicated by the vertical red lines.

pre-flare, at the peak of the Doppler flash, and post-flare with an RMdSE of 3.72 m/s and an MPE of 0.67%. From the data-model comparison in Figures 5 and 6, we conclude that the modeling framework, described in Section 3, can reproduce the Doppler phase shift experienced by a traveling radio wave through the modeled ionosphere reasonably accurately. Therefore, we can analyze the model outputs to gain insight into the driving mechanisms of Doppler flash.

To compare the evolution of ionospheric conditions following the solar flare, Figure 7 presents ionospheric electron density and propagation conditions along beam 7 of the Blackstone SuperDARN radar. As flare-driven photoionization produces large perturbations in the ionospheric electron density, we prefer to use electron density subtracted from the previous time instance, referred to as differential electron density ($\Delta n_e = n_e^{(t)} - n_e^{(t-1)}$), to better characterize ionospheric conditions. Top, middle, and bottom panels of Figure 7 present differential electron density, modeled Doppler velocity due to the change in refractive index, and modeled Doppler velocity due to the change in ray reflection height, respectively. The Doppler velocity estimation is done using Equations 1–3. Small popup panels at the bottom of the figure present the zoomed-in version of the rays presented in the panels (c-1 ~2). Left and right columns present simulation results before (22:03 UT) and during the solar flare (22:09 UT), respectively. Horizontal blue, orange, and red lines passing through panels (b) and (c) represent approximate lower boundaries of the D, E and F-regions, respectively. The blue dotted rays in panels (c-1 ~2) and (c-1 ~2:i) represent rays from the previous time step (t_{i-1}). The zoomed-in panels are added to provide a close-up look to compare the lowering of the F-region reflection height during pre-flare and flare times. The modeled result shows solar flare-driven electron density enhancement is predominantly in the E and F-regions. Specifically, the

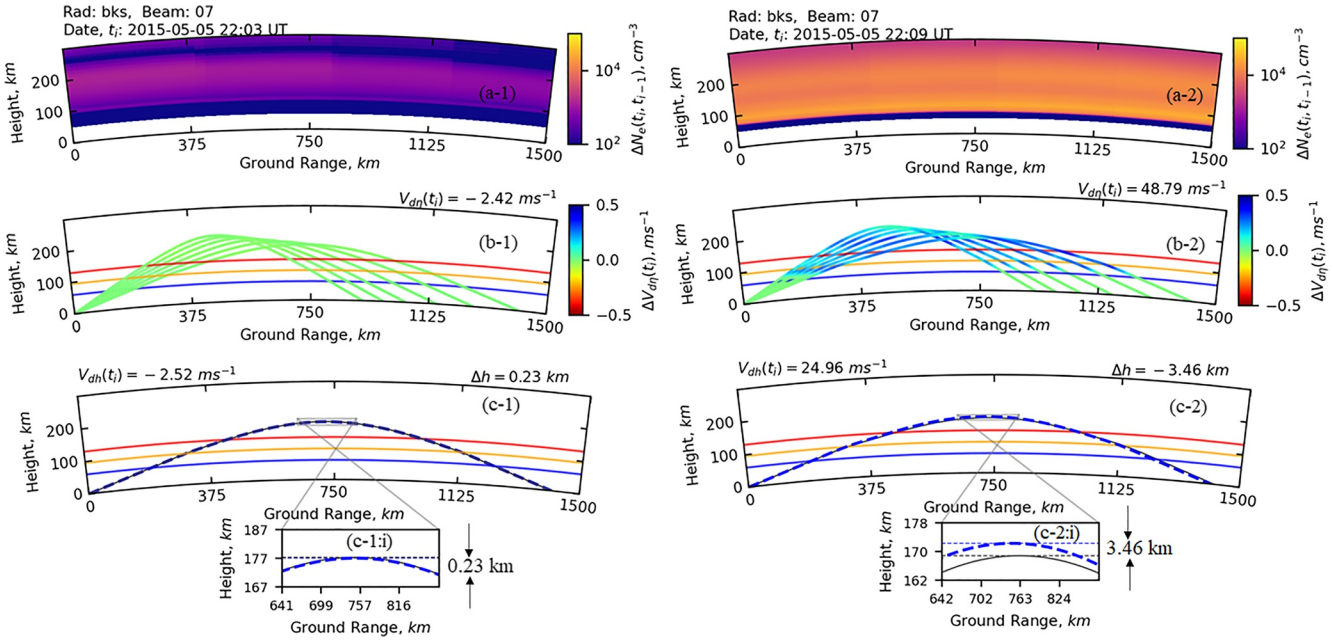

Figure 7. Change in the ionospheric electron density and the high frequency propagation condition along beam 7 of the SuperDARN Blackstone radar simulated using the model, before (at 22:03 UT) and during (at 22:09 UT) the solar flare on May 5, 2015: (a-1 ∼2) differential electron density (in cm^{-3}) simulated using the WACCM-X model color coded according to the scale on the right, (b-1 ∼2) modeled Doppler velocity along the transmitted rays due to the change in refractive index (in m/s) color coded according to the scale on the right, (c-1 ∼2) modeled Doppler velocity due to the change in ray reflection height (in m/s), and (c-1 ∼2:i) zoomed-in version of panel (c-1 ∼2) to show the drop in the F-region ray reflection point. Left and right columns present before and peak of the Doppler flash event. Dotted rays in panels (c-1 ∼2) and (c-1 ∼2:i) are the rays from the previous time stamp (t_{i-1}). Horizontal blue, orange, and red lines in panels (b) and (c) represent approximate lower boundaries of the D, E, and F-regions, respectively. Median Doppler velocity due to the change in refractive index and lowering of the F-region ray reflection height are provided in the top right corners of panels (b), and (c), respectively.

E-region electron density enhancement is more than the F-region enhancement, leading to an increase in Hall and Pedersen conductivities (Liu et al., 2020).

The simulation results presented in Figure 7 indicate that the rise in Doppler velocity is due to a decrease in refractive index as well as due to a lowering of the ray reflection height. By analyzing the pre-flare and flare-time propagation conditions, we find the following: during the solar flare (a) there is a significant enhancement in absolute electron density in the upper F and E-regions (deviative part of the ionosphere); (b) the change in Doppler velocity along the raypath due to change in refractive index is predominantly observed in the F and E-regions; and (c) the drop in ray reflection height is almost 3.46 km (refer to panel c-2:i) which is ∼15 times greater than the pre-flare condition that is, 0.23 km (refer to panel c-1:i) which is caused by the background change in the ionospheric propagation condition. The model framework outputs Doppler frequency shift driven by different ionospheric drivers and layers. The ratio between the Doppler frequency shift from individual driver to the total Doppler frequency shift is a measure of the relative contribution of that driver to the Doppler flash, which can be used to identify the major driver and its location in the ionosphere. The simulation suggests that, on average, relative contributions to the Doppler flash along beam 7 from the change in refractive index and lowering the F-region reflection height are $\frac{2}{3}$ and $\frac{1}{3}$, respectively. In addition, we found relative contributions to the Doppler flash from the D, E, and F-regions are ∼20%, ∼30%, and ∼50%, respectively. By analyzing the simulation results along beam 7 of the SuperDARN Blackstone radar, we found that both the change in refractive index and change in the ray reflection height contribute to the solar flare-driven Doppler flash. However, the change in refractive index is the dominant among the two factors under consideration. The simulation also shows that the F-region is the primary contributor to the Doppler flash.

To demonstrate further that the change in refractive index is the major driver and the F-region is the primary contributor to the Doppler flash, we conducted a statistical study based on the simulation results from all

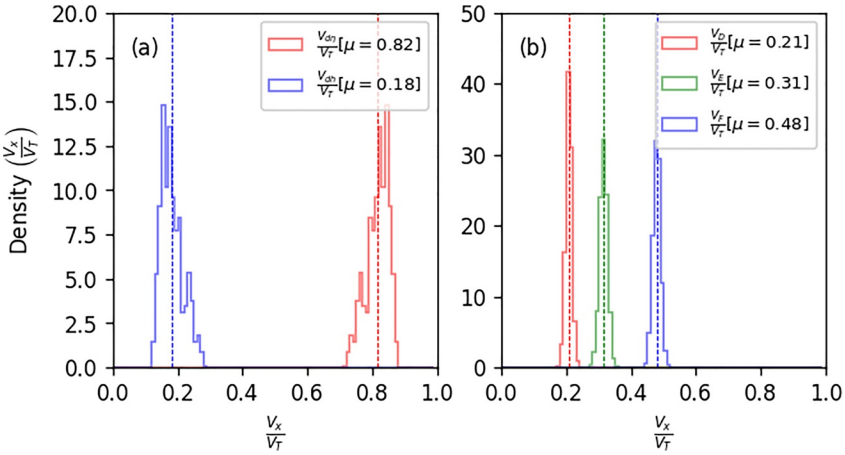

Figure 8. Histograms of (a) percentage of Doppler velocity contributed by the change in refractive index (in red) and change in ray reflection height (in blue), (b) percentage of Doppler velocity contributed by the D, E, and F-regions in red, green, and blue. Mean (μ) for each population is provided in the legend.

beams of the SuperDARN Blackstone radar. The estimations of percentage contributions by the ionospheric layers or the two factors to the Doppler flash mentioned in the previous paragraph use modeled values averaged along one beam of the Blackstone radar during the peak of the Doppler flash. In this statistical analysis we use simulated data for all beams (0–23), with different elevation angles (20°–35°), and during the whole period of Doppler flash observed by the radar (~ 22:07–22:09 UT), which gives ~1,080 simulated data points. Figure 8a presents histograms of relative contributions of the Doppler flash due to the change in refractive index (in red) and the change in ray reflection height (in blue). Figure 8b presents histograms of relative contributions of the Doppler flash by the D, E and F-regions in red, green and blue, respectively. Colored vertical dashed lines in both the panels represent the mean (μ) of each population. From the statistical analysis, we found that, on average, (a) relative contributions to the Doppler flash from the change in refractive index and change in the ray reflection height are ~82% and ~18%, respectively; and (b) relative contributions of D, E and F-regions are ~21%, ~31%, and ~48%, respectively. As HF rays are reflected at the F-region heights, therefore, among the total contribution by the F-region, ~18% is due to the change in ray reflection height and ~30% is due to the change in refractive index. Simulation results presented in Figure 7a shows that change in E-region electron density is larger than F-region density change. This suggests that the Doppler effect per unit traveling distance due to change in the refractive index on a traveling radio wave is higher in E-region than F-region. Figures 7b and 7c, which presents ray trace through the modified ionosphere, shows that the raypath is significantly larger in the F-region than that of the other two regions. Hence, the Doppler contributions by the E and F-regions due to the change in refractive index are comparable. Table 1 summarizes the percentage (%) contributions by the different ionospheric layers and drivers to Doppler flash, shows that the E and F-region contributions to change in refractive index are comparable. However, the F-region also contributes to Doppler flash via the change in the reflection height. Consequently, the F-region is the dominant driver of Doppler flash.

Table 1
Mean Percentage (%) Contributions by Different Ionospheric Layers and Drivers on the Doppler Flash, Modeled Using the Framework Described in Section 3 During a Solar Flare on May 5, 2015

	Total contribution to Doppler flash	Contribution from change in refractive index	Contribution from change in reflection height
D-region	21%	21%	0%
E-region	31%	31%	0%
F-region	48%	30%	18%
Whole Ionosphere	100%	82%	18%

4.3. Vertical Ion-Drift and the Change of the Ray Reflection Height

Prior studies have suggested that enhanced electron density due to photoionization caused by flare-increased EUVs and X-rays is a source of change in the ionospheric refractive index, which is the primary driver of the Doppler flash (Kikuchi et al., 1986; Watanabe & Nishitani, 2013). However, change in reflection height may also play a role. In a recent study, Chum et al. (2018) provided a mathematical construct of the Doppler frequency shift (f_D) observed by a normally incident radio wave:

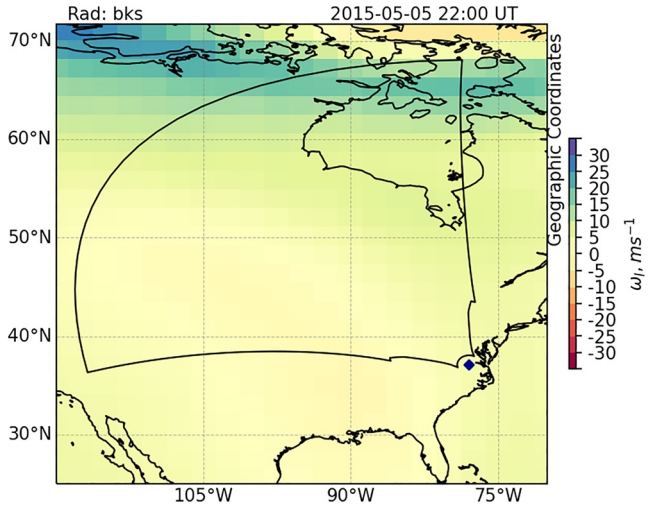

Figure 9. Vertical ion-drift velocity (ω_I) at 200 km altitude simulated using WACCM-X model before (at 22:00 UT) the solar flare on May 5, 2015. The velocity is color coded according to the scale on the right. The SuperDARN Blackstone radar's field-of-view is overlaid on top of the data.

$$f_D = -2.\frac{f}{c}\left(\int_0^h \frac{\partial \eta}{\partial n_e}\frac{\partial n_e}{\partial t}.dr\right) \quad (4)$$

where: c, η, n_e, h, and f are the speed of light, real part of the refractive index, electron density, ray reflection height, and frequency of the radio wave, respectively. The term $\frac{\partial n_e}{\partial t}$ indicates change in electron density, which can be contributed by various sources and can be decomposed using the equation of continuity as (Liu et al., 1996):

$$\frac{\partial n_e}{\partial t} = -\nabla n_e.\omega_I - n_e(\nabla.\omega_I) + p - l \quad (5)$$

where: ω_I, p, and l are vertical plasma-drift, electron production via photo ionization, and loss of free electrons. The first term of Equation 5 corresponds to vertical transport of plasma (advection) driven via $\vec{E} \times \vec{B}$ drift motion (Sutcliffe & Poole, 1989), while the second term represents plasma compression and rarefaction (Chum et al., 2016). During a solar flare the electron production rate in Equation 5 is predominantly controlled by photoionization, but we suggest vertical plasma-drift effect also contributes to the flare-driven Doppler flash via lowering the ray reflection height. We next present arguments and simulation results that support this contention.

Vertical ion-drift of the plasma is typically generated by the $\vec{E}_{zonal} \times \vec{B}_{meridional}$, where $\vec{E}_{zonal}$ and $\vec{B}_{meridional}$ are the east-west electric field and north-south magnetic field (Richmond et al., 1980). Typically, $\vec{B}_{meridional}$ in the mid-latitude northern hemisphere is northward directed and has a positive dip angle. In an observational study, Richmond et al. (1980) showed that during the summer season at ~17 LT (22 UT), $\vec{E}_{zonal}$ is weak and eastward directed resulting in a northward ion-flow (see Figure 1 in Richmond et al., 1980). Figure 9 presents the vertical ion-drift velocity (ω_I) simulated using the WACCM-X model at an altitude of 200 km during pre-solar flare (at 22:00 UT) conditions. The simulation result shows a slight positive (upward) motion of vertical ion-drift across the FoV of the Blackstone radar. This is consistent with a background zonal electric field that is, weak and uniform across the FoV of the radar.

To present the temporal evolution of vertical ion-drift during the initial phase of the flare-driven SID, Figure 10 presents the differential vertical ion-drift ($\Delta\omega_I$) at an altitude of 200 km. This is estimated by subtracting ω_I from the previous time stamp (t_{i-1}). The four panels of Figure 10 present differential vertical ion-drift velocity at 1-min cadence starting from 22:08 UT. This result is consistent with the results presented in Liu et al. (2020) and Qian et al. (2012), in that the weakening of vertical ion drift occurs in the initial phase following an X-class flare. With intensification of solar flare intensity through the rising phase of the event, there is a weakening effect on the upward motion of the ions that reduces the upward flow of plasma, which leads to an increased plasma density and, consequently, an increased Doppler frequency shift. The accumulation of plasma due to increased photoionization and decreased vertical outflow creates suitable conditions to reflect rays at relatively lower heights during solar flares than during quiet times. This suggests a flare-driven SID alters the background ionospheric current system that can be observed in ground magnetometer data as magnetic crochet (Rastogi et al., 1999).

5. Discussion

Kikuchi et al. (1986) first postulated a theory of the Doppler anomaly recorded in HF observations following solar flares and during geomagnetic storms. The study suggested two possible factors, manifested by two different geophysical phenomena: first, changes in refractive index of the non-deviative part of the ionosphere, the lower D and E-region, following a solar flare; second, changes in the F-region ray reflection height during a geomagnetic storm. In a more recent study, Watanabe and Nishitani (2013) showed that the change in the ionospheric refractive index is the major driver of the flare-driven Doppler flash. That study

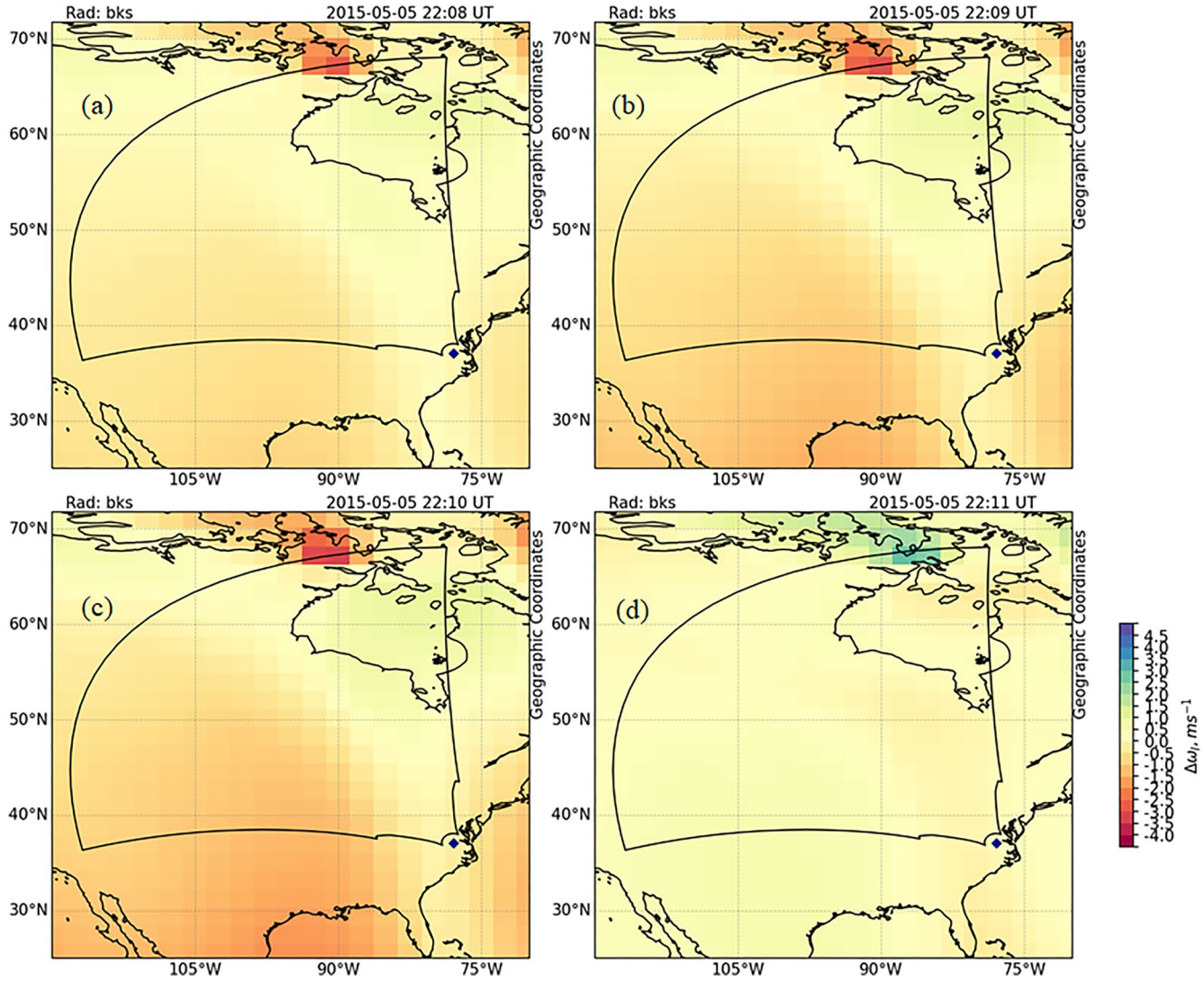

Figure 10. Differential vertical ion-drift velocity ($\Delta\omega_I$) from WACCM-X model at 200 km altitude during different phases of the flare evolution: (a) 22:08 UT, (b) 22:09 UT, (c) 22:10 UT, and (d) 22:11 UT. The difference uses 22:00 UT as the reference time.

used Doppler velocity observations from the SuperDARN Hokkaido radar to empirically validate their hypothesis. However, the study did not determine which region of the ionosphere is most responsible for the Doppler flash. We found, on average, the relative contributions from the change in ionospheric refractive index and the change in ray reflection height are ~82% and ~18%, respectively (refer to Figure 8). This indicates that the ionospheric refractive index is the major driver of the flare-driven Doppler flash, consistent with the conclusions of Watanabe and Nishitani (2013) and Kikuchi et al. (1986), respectively. In addition, statistical analysis suggests on average the F and E-regions contribute ~48% and ~31% of the flare-driven Doppler flash (refer to Figure 8), respectively. The relative contribution due to the change in refractive index and the change in ray reflection height on the F-region are ~30% and ~18%, respectively. Taking all of these results together, we can say the change in refractive index in the E and F-region is the major driver of the Doppler flash.

Another focus of this study was to investigate the sources of change in ray reflection point in the F-region following a solar flare. To our knowledge only a handful of prior studies have delved into this question for flare-driven SIDs. We found there are two factors which drive the lowering of the ray reflection height, first, the production of electrons via photoionization, and second, the weakening of the ionospheric vertical plasma-drift. The flare-enhanced refractive index forces rays to refract further and as a result they do not reach

as high compare to non-flare conditions. Sudden weakening of the ionospheric vertical ion-drift enhances plasma accumulation by reducing the vertical outflow of plasma at the F-region heights. A sudden reduction of vertical plasma motion at the low and middle latitude F-region could be driven by sudden change in the zonal electric field ($\vec{E}_{east}$) and (or) in the ionospheric conductivity (Curto et al., 2018; Liu et al., 2020).

Liu et al. (2020) examined mechanisms of weakened upward ion drift during the initial phase following an X-class solar flare. They found that sudden enhancements in electron density following solar flares increase both Hall and Pedersen conductivities. X-ray enhancements penetrate to lower heights to ionize the D and E region, while EUV dominates ionization at higher altitudes in the ionosphere F region. During X-class solar flares, soft and hard X-ray irradiances enhance ∼100 times more than EUV does. Consequently, electron density increases more at lower altitudes where the Hall conductivity resides and dominates. This increases the ratio of Hall to Pedersen conductance resulting in a large low-latitude increase in the Cowling conductance. In order to maintain global current continuity, the low-latitude zonal electric field must weaken during flares. The weakened eastward electric field causes weakened ionospheric vertical drift and weakened fountain effect during flares, as observed (Liu et al., 2020). The weakened ionospheric vertical drift changes the vertical distribution of plasma density, thus changing the radio signal reflection height. The sudden modification of ionospheric currents during flares also leads to the magnetic crochet effect (Rastogi et al., 1999).

6. Conclusions

In this study, we have presented a physics-based ray-tracing model framework for estimating the Doppler flash observed by the SuperDARN Blackstone radar following an X-class solar flare. We used the modeling results to gain insight about the generating mechanisms of the Doppler flash. We compared the relative contributions of two possible drivers of Doppler flash and the relative influence of the D, E, and F-regions. By analyzing and comparing the modeled estimates against observations, we found:

1. The model is able to reproduce the Doppler flash observation with an RMdSE of 3.72 m/s and a MPE of 0.67%.
2. Change in refractive index is the major driver of the Doppler Flash (∼82%).
3. The refractive index contribution to the Doppler flash is predominantly an E and F-region phenomenon.
4. Among the D, E, and F-regions, the F-region is the major contributor to the Doppler flash (∼48% in total: ∼18% is due to change in ray reflection height and ∼30% is due to a change in refractive index).
5. The apparent downward movement of the ray reflection height in the F-region is related to the increase in ionospheric refractive index and weakening of the vertical ion-drift.

For our future work, we will conduct a comprehensive statistical analysis using more solar flare events including M-class flares to find out whether these results apply to other solar flares in general.

Data Availability Statement

The majority of analysis and visualization was completed with the help of free, open-source software tools such as matplotlib (Hunter, 2007), IPython (Perez & Granger, 2007), pandas (McKinney, 2010), PyForecastTools (Morley, 2018), and others (e.g., Millman & Aivazis, 2011).

Acknowledgments
SC thanks to the HAO laboratory at NCAR for supporting the NCAR's Advanced Study Program's Graduate Student (GVP) Fellowship. SC also thanks to the National Science Foundation and the NASA for support under grant AGS-1935110 and 80NSSC20K1380, respectively. This material is based upon work supported by the National Center for Atmospheric Research, which is a major facility sponsored by the National Science Foundation under Cooperative Agreement No. 1852977. Any opinions, findings and conclusions or recommendations expressed in this material do not necessarily reflect the views of the National Science Foundation. We would like to acknowledge the use of computational resources (doi:10.5065/D6RX99HX) at the NCAR-Wyoming Supercomputing Center provided by the National Science Foundation and the State of Wyoming, and supported by NCAR's Computational and Information Systems Laboratory for the WACCM-X simulations. We wish to acknowledge the use of the NOAA/GOES X-ray data (from https://satdat.ngdc.noaa.gov/sem/goes/data/) for flare confirmation, analysis, and use as model inputs. We thank all participants in the worldwide SuperDARN collaboration for the distribution of SuperDARN data via http://vt.superdarn.org/tiki-index.php?page=Data+Access. The authors acknowledge Advanced Research Computing at Virginia Tech for providing computational resources and technical support that have contributed to the results reported within this paper (https://198.82.212.30).

References

Alken, P., & Maus, S. (2010). Relationship between the ionospheric eastward electric field and the equatorial electrojet. *Geophysical Research Letters*, *37*(4), L04104. https://doi.org/10.1029/2009GL041989

Cervera, M. A., & Harris, T. J. (2014). Modeling ionospheric disturbance features in quasi-vertically incident ionograms using 3-D magnetoionic ray tracing and atmospheric gravity waves. *Journal of Geophysical Research: Space Physics*, *119*(1), 431–440. https://doi.org/10.1002/2013JA019247

Chakraborty, S., Baker, J. B. H., Ruohoniemi, J. M., Kunduri, B., Nishitani, N., & Shepherd, S. G. (2019). A study of SuperDARN response to co-occurring space weather phenomena. *Space Weather*, *17*(9), 1351–1363. https://doi.org/10.1029/2019SW002179

Chakraborty, S., Ruohoniemi, J. M., Baker, J. B. H., & Nishitani, N. (2018). Characterization of short-wave fadeout seen in daytime SuperDARN ground scatter observations. *Radio Science*, *53*(4), 472–484. https://doi.org/10.1002/2017RS006488

Chamberlin, P. C., Woods, T. N., & Eparvier, F. G. (2007). Flare Irradiance Spectral Model (FISM): Daily component algorithms and results. *Space Weather*, *5*(7), S05001. https://doi.org/10.1029/2007SW000316

Chamberlin, P. C., Woods, T. N., & Eparvier, F. G. (2008). Flare Irradiance Spectral Model (FISM): Flare component algorithms and results. *Space Weather*, *6*(5), S05001. https://doi.org/10.1029/2007SW000372

Chisham, G., Lester, M., Milan, S. E., Freeman, M. P., Bristow, W. A., Grocott, A., et al. (2007). A decade of the Super Dual Auroral Radar Network (SuperDARN): Scientific achievements, new techniques and future directions. *Surveys in Geophysics*, *28*(1), 33–109. https://doi.org/10.1007/s10712-007-9017-8

Chum, J., Liu, J.-Y., Laštovička, J., Fišer, J., Mošna, Z., Baše, J., & Sun, Y.-Y. (2016). Ionospheric signatures of the April 25, 2015 Nepal earthquake and the relative role of compression and advection for Doppler sounding of infrasound in the ionosphere. *Earth, Planets and Space*, *68*(1), 24. https://doi.org/10.1186/s40623-016-0401-9

Chum, J., Urbář, J., Laštovička, J., Cabrera, M. A., Liu, J.-Y., Bonomi, F. A. M., et al. (2018). Continuous Doppler sounding of the ionosphere during solar flares. *Earth, Planets and Space*, *70*(1), 198. https://doi.org/10.1186/s40623-018-0976-4

Coleman, C. (1997). On the simulation of backscatter ionograms. *Journal of Atmospheric and Solar-Terrestrial Physics*, *59*(16), 2089–2099. https://doi.org/10.1016/S1364-6826(97)00038-2

Coleman, C. J. (1998). A ray tracing formulation and its application to some problems in over-the-horizon radar. *Radio Science*, *33*(4), 1187–1197. https://doi.org/10.1029/98RS01523

Curto, J. J., Marsal, S., Blanch, E., & Altadill, D. (2018). Analysis of the solar flare effects of 6 September 2017 in the ionosphere and in the Earth's magnetic field using spherical elementary current systems. *Space Weather*, *16*(11), 1709–1720. https://doi.org/10.1029/2018SW001927

Davies, K. (1990). *Ionospheric radio*. https://doi.org/10.1049/PBEW031E

Dellinger, J. H. (1937). Sudden ionospheric disturbances. *Terrestrial Magnetism and Atmospheric Electricity*, *42*(1), 49–53. https://doi.org/10.1029/TE042i001p00049

Ellison, M. A. (1953). The Hα radiation from solar flares in relation to sudden enhancements of atmospherics on frequencies near 27 Kc/s. *Journal of Atmospheric and Terrestrial Physics*, *4*(4–5), 226–239. https://doi.org/10.1016/0021-9169(53)90057-9

Fiori, R. A. D., Koustov, A. V., Chakraborty, S., Ruohoniemi, J. M., Danskin, D. W., Boteler, D. H., & Shepherd, S. G. (2018). Examining the potential of the Super Dual Auroral Radar Network for monitoring the space weather impact of solar X-ray flares. *Space Weather*, *16*(9), 1348–1362. https://doi.org/10.1029/2018SW001905

Fomichev, V. I., Kutepov, A. A., Akmaev, R. A., & Shved, G. M. (1993). Parameterization of the 15 μm CO_2 band cooling in the middle atmosphere (15-115 km). *Journal of Atmospheric and Terrestrial Physics*, *55*(1), 7–18. https://doi.org/10.1016/0021-9169(93)90149-S

Garcia, R. R., Marsh, D. R., Kinnison, D. E., Boville, B. A., & Sassi, F. (2007). Simulation of secular trends in the middle atmosphere, 1950–2003. *Journal of Geophysical Research*, *112*(D9), D09301. https://doi.org/10.1029/2006JD007485

Greenwald, R. A., Baker, K. B., Hutchins, R. A., & Hanuise, C. (1985). An HF phased-array radar for studying small-scale structure in the high-latitude ionosphere. *Radio Science*, *20*(1), 63–79. https://doi.org/10.1029/RS020i001p00063

Hansen, R., & Kleczek, J. (1962). Coincidence of Sudden Ionospheric Disturbances with the Explosive Phase of Solar Flares. *Nature*, *195*(4848), 1280–1281. https://doi.org/10.1038/1951280a0

Haselgrove, J. (1963). The Hamiltonian ray path equations. *Journal of Atmospheric and Terrestrial Physics*, *25*(7), 397–399. https://doi.org/10.1016/0021-9169(63)90173-9

Heelis, R. A., Lowell, J. K., & Spiro, R. W. (1982). A model of the high-latitude ionospheric convection pattern. *Journal of Geophysical Research*, *87*(A8), 6339–6345. https://doi.org/10.1029/JA087iA08p06339

Hunter, J. D. (2007). Matplotlib: A 2D graphics environment. *Computing in Science & Engineering*, *9*(3), 90–95. https://doi.org/10.1109/MCSE.2007.55

Hurrell, J. W., Holland, M. M., Gent, P. R., Ghan, S., Kay, J. E., Kushner, P. J., et al. (2013). The community Earth system model: A framework for collaborative research. *Bulletin of the American Meteorological Society*, *94*(9), 1339–1360. https://doi.org/10.1175/BAMS-D-12-00121.1

Khan, I., Devi, M. I., Arunamani, T., & Madhusudhana Rao, D. N. (2005). A synoptic study of VLF sudden phase anomalies recorded at Visakhapatnam. *Earth, Planets and Space*, *57*(11), 1073–1081. https://doi.org/10.1186/BF03351886

Kikuchi, T., Sugiuchi, H., Ishimine, T., Maeno, H., & Honma, S. (1986). Solar-terrestrial disturbances of June-September 1982, IV. Ionospheric disturbances, 11. HF Doppler observations. *Journal of the Radio Research Laboratory*, *33*(1), 239–255.

Kinnison, D. E., Brasseur, G. P., Walters, S., Garcia, R. R., Marsh, D. R., Sassi, F., et al. (2007). Sensitivity of chemical tracers to meteorological parameters in the MOZART-3 chemical transport model. *Journal of Geophysical Research*, *112*(D20), D20302. https://doi.org/10.1029/2006JD007879

Liu, H.-L., Bardeen, C. G., Foster, B. T., Lauritzen, P., Liu, J., Lu, G., et al. (2018). Development and validation of the whole atmosphere community climate model with thermosphere and ionosphere extension (WACCM-X 2.0). *Journal of Advances in Modeling Earth Systems*, *10*(2), 381–402. https://doi.org/10.1002/2017MS001232

Liu, H.-L., Foster, B. T., Hagan, M. E., McInerney, J. M., Maute, A., Qian, L., et al. (2010). Thermosphere extension of the whole atmosphere community climate model. *Journal of Geophysical Research*, *115*(A12), A12302. https://doi.org/10.1029/2010JA015586

Liu, J., Liu, H., Wang, W., Burns, A. G., Wu, Q., Gan, Q., et al. (2018). First results from the ionospheric extension of WACCM-X during the deep solar minimum year of 2008. *Journal of Geophysical Research: Space Physics*, *123*(2), 1534–1553. https://doi.org/10.1002/2017JA025010

Liu, J., Qian, L., Maute, A., Wang, W., Richmond, A. D., Chen, J., et al. (2020). Electrodynamical coupling of the geospace system during solar flares. *Journal of Geophysical Research: Space Physics*, *125*, e2020JA028569. https://doi.org/10.1029/2020JA028569

Liu, J. Y., Chiu, C. S., & Lin, C. H. (1996). The solar flare radiation responsible for sudden frequency deviation and geomagnetic fluctuation. *Journal of Geophysical Research*, *101*(A5), 10855–10862. https://doi.org/10.1029/95JA03676

Lu, G., & Richmond, A. D. (1996). Specification and forecast of ionospheric conditions with AMIE. In *The evaluation of space weather forecasts* (pp. 35–38).

Marsh, D. R., Mills, M. J., Kinnison, D. E., Lamarque, J.-F., Calvo, N., & Polvani, L. M. (2013). Climate change from 1850 to 2005 simulated in CESM1(WACCM). *Journal of Climate*, *26*(19), 7372–7391. https://doi.org/10.1175/JCLI-D-12-00558.1

McKinney, W. (2010). Data structures for statistical computing in Python. In S. van der Walt, & J. Millman (Eds.), *Proceedings of the 9th Python in science conference* (pp. 56–61). https://doi.org/10.25080/Majora-92bf1922-012

Mendillo, M., & Evans, J. V. (1974). Incoherent scatter observations of the ionospheric response to a large solar flare. *Radio Science*, *9*(2), 197–203. https://doi.org/10.1029/RS009i002p00197

Millman, K. J., & Aivazis, M. (2011). Python for Scientists and Engineers. *Computing in Science & Engineering*, *13*(2), 9–12. https://doi.org/10.1109/MCSE.2011.36

Morley, S. (2018). *drsteve/PyForecastTools: PyForecastTools*. https://doi.org/10.5281/zenodo.1256921

Neale, R. B., Richter, J., Park, S., Lauritzen, P. H., Vavrus, S. J., Rasch, P. J., & Zhang, M. (2013). The mean climate of the Community Atmosphere Model (CAM4) in forced SST and fully coupled experiments. *Journal of Climate*, *26*(14), 5150–5168. https://doi.org/10.1175/JCLI-D-12-00236.1

Nishitani, N., Ruohoniemi, J. M., Lester, M., Baker, J. B. H., Koustov, A. V., Shepherd, S. G., et al. (2019). Review of the accomplishments of mid-latitude Super Dual Auroral Radar Network (SuperDARN) HF radars. *Progress in Earth and Planetary Sciences*, *6*(1), 27. https://doi.org/10.1186/s40645-019-0270-5

Pedatella, N. M., Chau, J. L., Vierinen, J., Qian, L., Reyes, P., Kudeki, E., et al. (2019). Solar flare effects on 150-km echoes observed over Jicamarca: WACCM-X simulations. *Geophysical Research Letters*, *46*(20), 10951–10958. https://doi.org/10.1029/2019GL084790

Pedatella, N. M., Liu, H.-L., Marsh, D. R., Raeder, K., Anderson, J. L., Chau, J. L., et al. (2018). Analysis and hindcast experiments of the 2009 sudden stratospheric warming in WACCMX+DART. *Journal of Geophysical Research: Space Physics*, *123*(4), 3131–3153. https://doi.org/10.1002/2017JA025107

Perez, F., & Granger, B. E. (2007). Ipython: A system for interactive scientific computing. *Computing in Science & Engineering*, *9*(3), 21–29. https://doi.org/10.1109/MCSE.2007.53

Qian, L., Burns, A. G., Solomon, S. C., & Chamberlin, P. C. (2012). Solar flare impacts on ionospheric electrodynamics. *Geophysical Research Letters*, *39*(6), L06101. https://doi.org/10.1029/2012GL051102

Qian, L., Burns, A. G., Solomon, S. S., Smith, A. K., McInerney, J. M., Hunt, L. A., et al. (2018). Temporal variability of atomic hydrogen from the mesopause to the upper thermosphere. *Journal of Geophysical Research: Space Physics*, *123*(1), 1006–1017. https://doi.org/10.1002/2017JA024998

Rastogi, R. G., Pathan, B. M., Rao, D. R. K., Sastry, T. S., & Sastri, J. H. (1999). Solar flare effects on the geomagnetic elements during normal and counter electrojet periods. *Earth, Planets and Space*, *51*(9), 947–957. https://doi.org/10.1186/BF03351565

Richmond, A. (1992). Assimilative mapping of ionospheric electrodynamics. *Advances in Space Research*, *12*(6), 59–68. https://doi.org/10.1016/0273-1177(92)90040-5

Richmond, A. D., Blanc, M., Emery, B. A., Wand, R. H., Fejer, B. G., Woodman, R. F., et al. (1980). An empirical model of quiet-day ionospheric electric fields at middle and low latitudes. *Journal of Geophysical Research*, *85*(A9), 4658–4664. https://doi.org/10.1029/JA085iA09p04658

Siskind, D. E., Zawdie, K. A., Sassi, F., Drob, D., & Friedrich, M. (2017). Global modeling of the low- and middle-latitude ionospheric D and lower E Regions and implications for HF radio wave absorption. *Space Weather*, *15*(1), 115–130. https://doi.org/10.1002/2016SW001546

Solomon, S. C., Liu, H.-L., Marsh, D. R., McInerney, J. M., Qian, L., & Vitt, F. M. (2018). Whole atmosphere simulation of anthropogenic climate change. *Geophysical Research Letters*, *45*(3), 1567–1576. https://doi.org/10.1002/2017GL076950

Solomon, S. C., Liu, H.-L., Marsh, D. R., McInerney, J. M., Qian, L., & Vitt, F. M. (2019). Whole atmosphere climate change: Dependence on solar activity. *Journal of Geophysical Research: Space Physics*, *124*(5), 3799–3809. https://doi.org/10.1029/2019JA026678

Solomon, S. C., & Qian, L. (2005). Solar extreme-ultraviolet irradiance for general circulation models. *Journal of Geophysical Research*, *110*(A10), A10306. https://doi.org/10.1029/2005JA011160

Sumod, S. G., & Pant, T. K. (2019). An investigation of solar flare effects on equatorial ionosphere and thermosphere using co-ordinated measurements. *Earth, Planets and Space*, *71*(1), 125. https://doi.org/10.1186/s40623-019-1105-8

Sutcliffe, P. R., & Poole, A. W. V. (1989). Ionospheric Doppler and electron velocities in the presence of ULF waves. *Journal of Geophysical Research*, *94*(A10), 13505–13514. https://doi.org/10.1029/JA094iA10p13505

Watanabe, D., & Nishitani, N. (2013). Study of ionospheric disturbances during solar flare events using the SuperDARN Hokkaido radar. *Advances in Polar Science*, *24*(1), 12–18. https://doi.org/10.3724/SP.J.1085.2013.00012

Weimer, D. R. (2005). Improved ionospheric electrodynamic models and application to calculating joule heating rates. *Journal of Geophysical Research*, *110*(A5), A05306. https://doi.org/10.1029/2004JA010884